Advanced Optical Materials

ADVANCED OPTICAL MATERIALS
www.advopticalmat.de

RESEARCH ARTICLE OPEN ACCESS

Near-Field Nanoimaging of Programmable Phase Transitions in Ga^+-Irradiated VO_2

Sarabpreet Singh[1] | Nareg Ghazikhanian[2] | Muhammad Asjad[1] | Erbin Qiu[2] | Ivan K. Schuller[2] | Yohannes Abate[1]

[1]Department of Physics and Astronomy, University of Georgia, Athens, Georgia, USA | [2]Department of Physics, University of California San Diego, La Jolla, California, USA

Correspondence: Yohannes Abate (yohannes.abate@uga.edu)

Received: 31 March 2026 | **Revised:** 18 August 2026 | **Accepted:** 22 August 2026

Keywords: ion beam irradiation | materials science | near-field imaging | neuromorphic engineering | optoelectronics | phase transition

ABSTRACT

Developing quantum materials for electronic devices, including neuromorphic computing, is a rapidly expanding field. Vanadium dioxide (VO_2) is a prototypical correlated oxide known for its sharp, reversible insulator-to-metal transition (IMT), making it a compelling platform for reconfigurable electronics. Controlled defect formation, such as focused Ga^+ ion beam irradiation, can influence the IMT in VO_2, yet the associated nanoscale phase behavior and switching mechanisms remain largely unexplored. Here we introduce spatially localized defects in VO_2 using focused Ga^+ irradiation with tunable dose and probe the resulting thermal- and voltage-driven IMT using infrared and terahertz near-field nano-imaging. Focused Ga^+ irradiation alters, and often suppresses, phase switching behavior, localizing the conductive pathway and reducing switching power for energy-efficient neuromorphic functionality. Compared to pristine VO_2, the irradiated material exhibits suppressed IMT behavior, with lower resistivity below the transition temperature but higher resistivity above it. Varying irradiation dose modulates this suppression, impacting filamentary nucleation. Devices with lightly irradiated regions localize the resistive switching behavior, whereas heavily irradiated regions remained inactive during switching, with neighboring pristine material switching into the metallic phase instead. These findings reveal selective ion irradiation enables local control of the IMT in VO_2, offering a scalable route to programmable, energy-efficient neuromorphic devices.

1 | Introduction

Engineering quantum materials for electronic device applications, especially in areas like neuromorphic computing [1–7] and adaptive electronics [8–10], is a rapidly growing field. These materials exhibit emergent properties that can be tailored through defect creation, strain, or compositional modulation to enable reconfigurable, low-power and high-performance functionalities. Transition metal dichalcogenides (TMDs) [11–13] and correlated oxides like vanadium dioxide (VO_2) [14–16] are among such materials actively explored for these purposes. Techniques such as ion implantation, interfacial control, and nanoscale patterning offer new ways to manipulate electronic phase, conductivity, and switching behavior at the device level.

VO_2 is a widely studied correlated oxide known for its insulator-to-metal transition (IMT) [17] near room temperature [18]. The IMT has been extensively investigated over several decades, yet it continues to reveal new complexities [6, 17–19]. The transition temperature (T_c) and other phase characteristics of VO_2 can be significantly modified through doping, strain, intercalation, or irradiation [19–24], making it a versatile platform for exploring phase-transition-based functionalities in nanoscale devices. Many stimuli can drive the IMT, including temperature and

applied electric field [17, 18]. In VO_2, the application of sufficient current or voltage can locally trigger the IMT, leading to the formation of a percolating conducting filament in a process known as volatile resistive switching [6, 8]. Once the stimulus is removed, the material rapidly relaxes back to its insulating state [25].

An exciting application of VO_2 lies in neuromorphic computing, where it can mimic the key functionalities of neurons, including leaky-integrate-and-fire [25], through its IMT behavior. This intrinsic ability can be used to store and process information [26, 27] in a dynamic and energy-efficient manner, making VO_2 an ideal candidate for brain-inspired hardware. One promising approach to control the IMT is through focused ion beam [28, 29] (FIB) irradiation, which can locally define metallic and insulating domains in the material [14, 30–33]. This technique has been employed to realize memristive devices with tunable switching characteristics. However, despite its potential, much of the nanoscale physics in irradiated VO_2 remains poorly understood due to the lack of methods that can resolve both surface and subsurface conductivity with high spatial resolution.

In this work, we use IR and THz near-field nanoimaging [34] to investigate how focused Ga^+ ion beam irradiation modulates the phase transition and electronic behavior of VO_2 thin films. By systematically varying the ion dose (0.2–50 pC μm^{-2}), we introduce well-defined nanoscale defects and track the resulting changes in local and global device properties. Both thermally- and electrically- driven phase switching are spatially resolved using scattering-type scanning near-field optical microscopy [34, 35] (s-SNOM) with harmonic-dependent imaging, which distinguishes surface and subsurface features. Low-dose Ga^+ irradiated regions exhibit increased metallic behavior at room temperature compared to pristine VO_2 and retain phase transition characteristics similar to pristine VO_2, whereas regions irradiated with high-dose Ga^+ display suppressed switching and insulating behavior, unlike the IMT of the pristine VO_2. These findings highlight how local defect engineering can program phase behavior and conductivity at the nanoscale, providing insight for the design of energy efficient reconfigurable VO_2-based devices in neuromorphic systems.

2 | Results and Discussion

Vanadium dioxide (VO_2) thin films with thickness 40 nm were fabricated using radio frequency (RF) magnetron sputtering on (1 0 2)-oriented Al_2O_3 substrates [14]. The deposition of VO_2 thin films was conducted in an atmosphere of 3.6 mTorr of Ar/O_2 (93/7%) at a substrate temperature of 470°C, employing reactive RF magnetron sputtering from a V_2O_3 target. Following deposition, the VO_2 samples were preserved in the same atmosphere and cooled at a rate of 12°C per minute. Figure 1a shows the schematic of a focused ion beam creating defects in the VO_2 film using a 30 keV Ga^+ ion dose. FIB [28] irradiation provided a controllable way to introduce structural defects into VO_2 film by adjusting the ion fluence. Figure 1b and Figure S1 depict the estimated depth-dependent ion trajectory distribution for 30 keV Ga^+ ions implanted into a VO_2 thin film, simulated using the Monte Carlo code Transport of Ions in Matter (TRIM) [36–38]. The X-axis denotes penetration depth, while the Y-axis represents lateral spread perpendicular to an incident point source. Figure S2 shows the density of Ga^+ ions implanted into the VO_2 film, which we estimated using TRIM [30, 36] simulations for 0.2 and 50 pC μm^{-2} dose of Ga^+ ions on VO_2 film. The vertical axis indicates the Ga^+ density (10^{20} cm^{-3}), while the horizontal axis shows the implantation depth (nm) into the VO_2 layer. The profile exhibits a non-monotonic behavior, with Ga^+ density first increasing with depth, reaching a maximum at ≈20 nm, and then decreasing. This characteristic shape results from the interplay between electronic and nuclear stopping processes during implantation: at shallow depths, Ga^+ ions retain sufficient kinetic energy to traverse the lattice with minimal scattering, whereas at intermediate depths, increased nuclear collisions promote ion capture and implantation. Beyond the peak, the drop in Ga^+ density indicates a lack of ion kinetic energy, therefore ending the penetration process. Each incident Ga^+ ion generates hundreds of lattice displacements, with oxygen vacancies (Figure S3) being the dominant defect species. The inset of Figure 1b shows the vacancies created per incident ion in VO_2 film when irradiated by Ga^+ ions using a 30 keV ion source. Other works have also shown that irradiation with different ion species produces similar effect in VO_2, reinforcing defect creation as the primary mechanism [14, 30, 33, 39]. In particular, O^+ irradiation has been shown to produce similar changes in the transport behavior of VO_2 despite introducing oxygen into the material, indicating that the irradiation response is not governed by stoichiometric modification alone [39]. Consistently, TRIM simulations of Ga^+-irradiated V_2O_3 have shown that each incident Ga^+ ion can generate hundreds of atomic displacements throughout the film thickness, further highlighting the important role of collision-induced lattice defects in modifying the electronic response [40]. This implantation profile directly defines the spatial distribution of Ga-induced defects, mainly oxygen vacancies, within the VO_2 film, crucial for tailoring its optical and electronic properties via defect engineering.

Figure 1c displays the resistance versus temperature (blue curve) and the resistance versus applied voltage performed at room temperature ≈300K (red curve) for the VO_2 device which shows the temperature-driven insulator-to-metal phase transition and volatile resistive switching, respectively. Both measurements display characteristic features of a first-order phase transition, including coexistence of phases and hysteresis loops, consistent with previous studies [5, 6, 14, 41–43]. The Ga^+-irradiated VO_2 device is then investigated using IR and THz s-SNOM (schematic shown in Figure 1d), which provide sub-diffraction spatial profiles of the electronic phase of the device when exposed to voltage or temperature. A light-irradiated s-SNOM tip is brought into close proximity to the sample surface, and the scattered light is collected at higher harmonics of the tip's oscillation frequency. Raster scanning the sample yields spatially resolved near-field images at a single excitation frequency (Figure 1e-i–iii), revealing the conductivity profile with spatial resolution limited by the tip apex radius (typically < 50 nm). The lateral resolution, as well as the depth composition profiling, are harmonic-order-dependent. In Figure 1e-iv, the second harmonic signal is large due to larger probe volume, and the signal progressively weakens with increasing harmonic order (schematic shown in Figure 1d), while simultaneously the near-field is spatially more confined with increasing harmonic order.

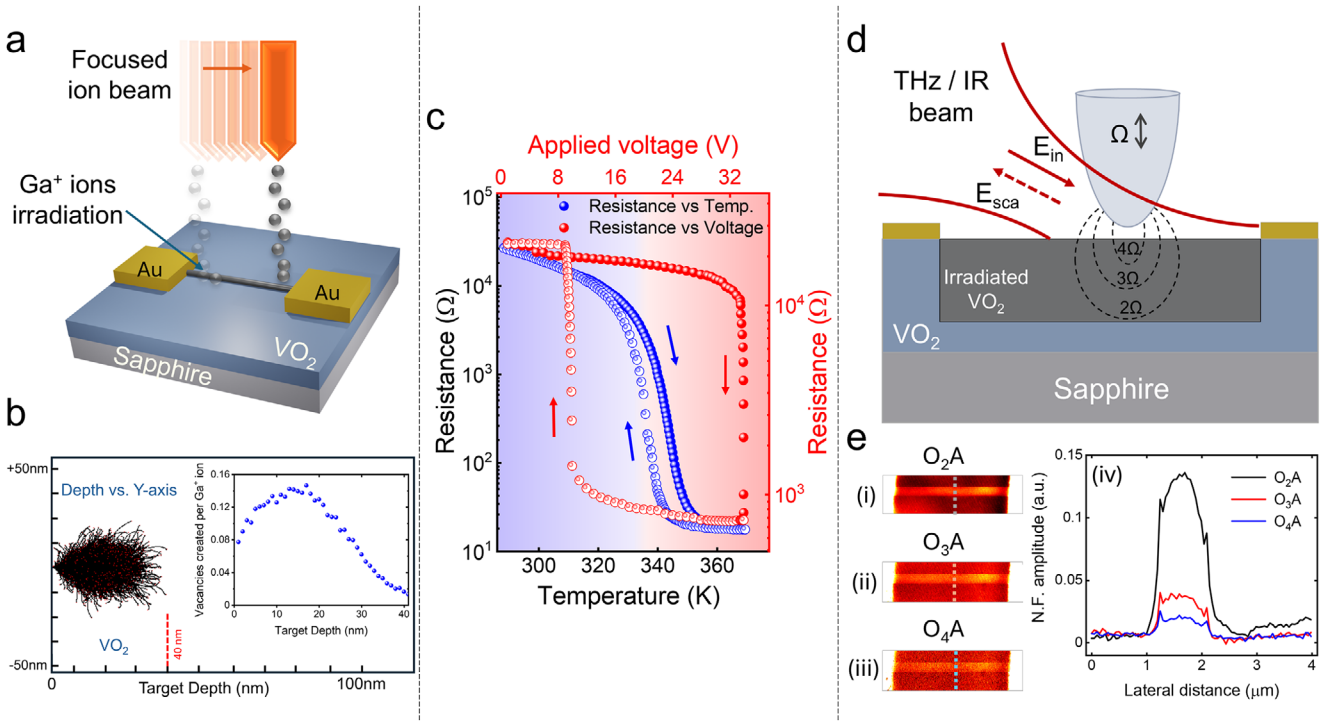

FIGURE 1 | (a) Schematic of the FIB-assisted Ga^+ ion irradiation setup; the sample is a VO_2 thin-film device on a R-cut sapphire substrate. (b) SRIM simulation of the experimental conditions using 30 keV Ga^+ ion implantation on a 40 nm thick VO_2 film, showing the Ga^+ ion distribution of implanted ions as a function of penetration depth along the ion beam direction and lateral (Y-axis) displacement transverse to the beam. The dashed line at 40 nm indicates the experimental VO_2 film boundary. Inset: simulated vacancies created per Ga^+ ion as a function of target sample depth. (c) Resistance vs temperature (blue curves) and resistance vs. applied voltage at room temperature (red curves) for VO_2 devices irradiated with a 1 μm wide strip of Ga^+ ions using a dose of 0.2 pC μm^{-2}. (d) Schematic of the s-SNOM experimental setup: a metal-coated AFM tip illuminated with IR or THz beam near the VO_2 device. The dashed lines surrounding the tip apex illustrate the probing regions associated with different harmonics (nΩ, where Ω denotes the tip oscillation frequency). (e) Near-field amplitude images and corresponding line profiles of the Ga^+-irradiated VO_2 film at 314 K, recorded at various harmonics using an excitation laser frequency of 952 cm^{-1}.

We performed infrared nanoimaging to investigate the phase transition and the nanoscale conductivity profile of varying Ga^+ ion irradiated VO_2 thin film devices as a function of temperature. Figure 2a–c and Figure S4d–f show the third harmonic IR amplitude images taken at a laser frequency of 952 cm^{-1} of three devices exposed to 0.2, 10, and 50 pC μm^{-2} Ga^+ doses at different temperatures. The images reveal various degrees of the electronic phase transition of VO_2 and remarkable differences in nanoscale conductivity for varying Ga^+ irradiation doses, inducing localized defect formations. To elucidate these changes in Figure 2d–f, we plotted normalized third harmonic amplitude values as a function of temperature on the Ga^+ ion irradiated area (blue curve) and on the pristine VO_2 film without irradiation (green curve). The signal is acquired from the blue and green points shown in panel (i) of Figure 2a–c and normalization was performed relative to the signal on the gold electrode (black dots). The irradiated regions (blue) for the three different devices with 0.2, 10, and 50 pC μm^{-2} Ga^+ doses show profoundly different phase transition behavior than the pristine (green) VO_2 film when heated to ≈353 K (above $T_c \approx 340$ K). The normalized amplitude values at room temperature (304 K) are higher for Ga^+ irradiated regions compared to the pristine film for all devices we measured, indicating the irradiated region is more conductive in the insulating state than the as-grown VO_2. This is noteworthy since it implies that Ga^+ irradiation can create conductive paths for directing current flow; a useful feature which could enable energy minimization in neuromorphic applications. However, when the base temperatures (340K, and 353K) are close to the transition temperature or above, the irradiated regions for all devices display lower amplitudes and thus become less metallic compared to the metallic state of the pristine film at the same temperature. This indicates that the Ga^+ irradiation makes the insulating phase more conductive and the metallic phase more resistive.

Interestingly, while the 0.2 pC μm^{-2} device still transitions in a similar trend as the pristine region (though it transitions less and the metallic state resistance of the irradiated region is still higher than the metallic state resistance of the pristine film at the same temperature). The devices with larger doses: 10 pC μm^{-2}, and 50 pC μm^{-2} show complete suppression of the electronic phase transition in the irradiated region. These results clearly show that irradiation with varying dose of Ga^+ significantly changes both the local, room-temperature conductivity as well as the IMT switching of VO_2 films. Furthermore, the Ga^+ irradiation perturbs adjacent "pristine" VO_2, as evidenced by the decrease in its normalized amplitude with increasing dose, indicating that elastic strain and/or irradiation-induced point defects from the damaged region may influence the neighboring pristine film.

Figure 2g–i shows near-field amplitude images and corresponding line profiles along the irradiated regions, normalized to the Au

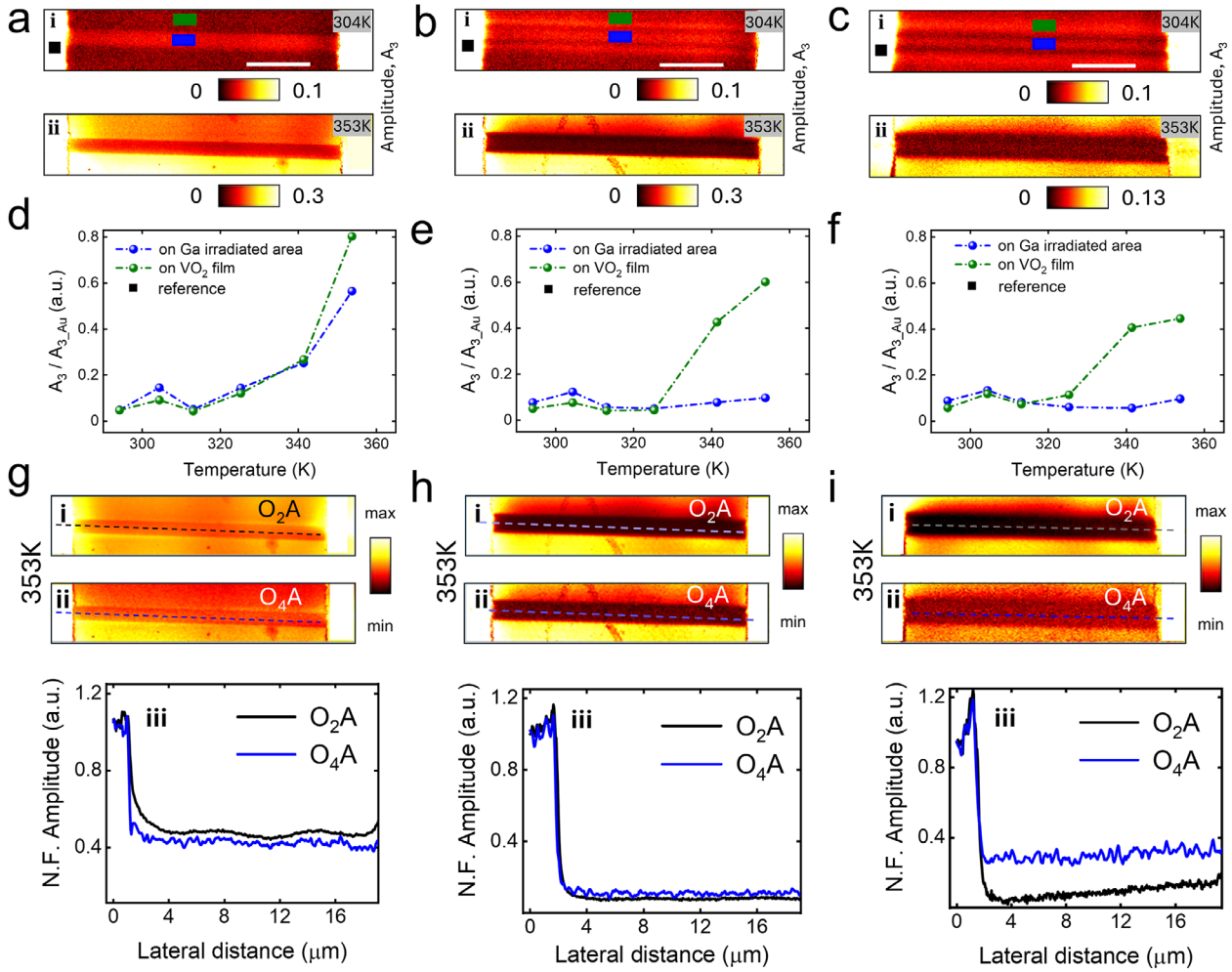

FIGURE 2 | Infrared imaging of temperature-dependent nanoscale conductivity profiles of VO_2 devices irradiated with varying Ga^+ ion doses. (a–c) Third harmonic near-field IR amplitude images of VO_2 films taken at a laser frequency of 952 cm^{-1}, showing the effects of three different Ga^+ ion irradiation doses at two temperatures: (i) 304.4 K (below T_c) and (ii) 353.8 K (above T_c). (d–f) Normalized third harmonic near-field amplitude signals from regions irradiated with Ga^+ ions (blue points) and non-irradiated regions (green points), plotted as a function of temperature for devices subjected to different irradiation doses. The connecting lines serve as guides to the eye. The blue and green points marked in panel (i) of (a–c) denote the locations from which the blue and green curves were extracted, with normalization performed relative to the signal on the gold electrode (black dot). Scale bars represent 4 μm. (g–i) Second (i) and fourth (ii) harmonic amplitude images of VO_2 devices irradiated with varying Ga^+ ion doses and their corresponding line profiles (iii), all acquired at a laser frequency of 952 cm^{-1}.

electrode and taken from the marked locations in the amplitude images. The difference in Ga^+ irradiation dose is reflected in the harmonic-dependent near-field amplitude contrast. In the lightly irradiated device (0.2 pC μm^{-2}), the fourth harmonic signal, being more surface-sensitive, exhibits greater contrast than the second harmonic signal, as shown by the blue and black line profiles respectively in Figure 2g-iii. In contrast, for the heavily irradiated device (50 pC μm^{-2}), the irradiation induces a greater concentration of defects more deeply into the sample, and the second harmonic signal, being more sensitive to subsurface features, shows stronger contrast than the fourth harmonic, as shown by the black and blue line profiles in Figure 2i-iii. The near-field harmonic responses imply that, although the Ga^+ irradiation depth remains roughly comparable across doses, the resulting defect concentration landscape does not. Higher irradiation doses promote the formation of a larger defect population that extends deeper into the VO_2 film, indicating that the harmonics are sensitive to subsurface defect profiles and not just to the nominal penetration depth.

Line profiles in Figure S5d–f, derived from the third harmonic amplitude images along the white dashed lines in Figure S5a–c, reveal spatial variations in conductivity across the irradiated regions, independent of Ga^+ dose. These variations could arise from dose exposure non-uniformity and inhomogeneities produced during growth or self-induced strain [24]. As temperature increases, the profiles become more uniform, as shown in Figure S3, due to an increase in the metallic phase fraction that smooths conductivity differences.

We further investigate how varying local doses of Ga^+ ion irradiation affect voltage-induced resistive switching characteristics using infrared near-field nanoimaging. Figure 3a,b display near-field amplitude images for a lightly irradiated (0.2 pC μm^{-2}) and heavily irradiated (50 pC μm^{-2}) devices at the room temperature (≈300K). The corresponding normalized near-field signal plots as a function of voltage are shown in Figure 3c,d for each device. In Figure 3a, for the 0.2 pC μm^{-2} device at 0 V, the

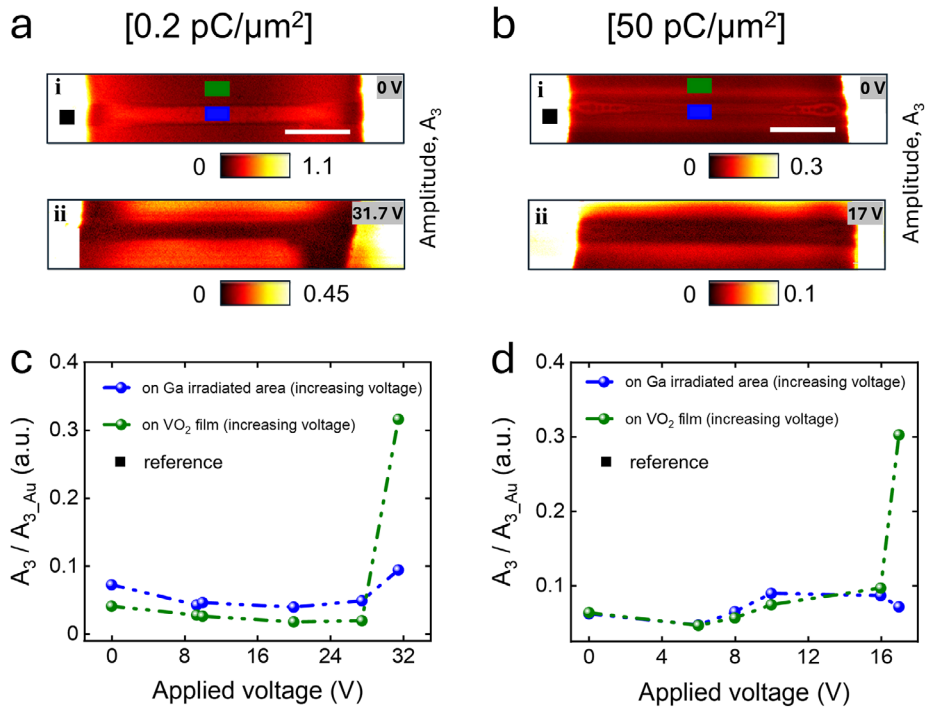

FIGURE 3 | Nanoscale infrared profiling of voltage response of VO_2 devices irradiated with Ga^+ ions. Near-field amplitude images for voltage-induced resistive switching in devices irradiated with a dose of (a) 0.2 pC μm^{-2} and (b) 50 pC μm^{-2}. The comparison of normalized third harmonic amplitude responses to voltage changes for Ga^+-irradiated and pristine VO_2 films is shown in (c) for the sample with a 0.2 pC μm^{-2} dose and in (d) for the sample with a 50 pC μm^{-2} dose, where the blue dashed lines represent data taken at Ga^+-irradiated region and the green dashed lines represent data taken pristine VO_2 film. Scale bars indicate 4 μm.

third harmonic amplitude image shows bright contrast in the irradiated area compared to the rest of the pristine VO_2 film, indicating the irradiated region is more metallic than the pristine region below T_c. However, as the applied voltage reaches the transition voltage of 31.7 V and the device undergoes resistive switching (see IV curve in Figure S8a), the contrast reverses, and the irradiated area becomes darker than the pristine VO_2 region. The relatively high transition voltage arises primarily from the approximately 18 μm electrode separation required for near-field scanning, while scaled devices with shorter channels are expected to operate at substantially lower voltages. These images show that the irradiated region has a lower room temperature resistivity than the pristine region, which can dominate current conduction. Due to the voltage-controlled measurement, the voltage across the device must remain the same after switching, indicating that the VO_2 device switches deeply into the metallic state, forming a very wide filament that extends beyond the irradiated region. Thus, both the pristine and irradiated regions undergo resistive switching, and the metallic phase of the irradiated region is more resistive than the metallic phase of the pristine region.

To further analyze voltage controlled near-field measurements, we plotted the normalized near-field amplitude signal from the irradiated region in the 0.2 pC μm^{-2} (Figure 3c) and 50 pC μm^{-2} devices (Figure 3d). Consistent with the temperature-driven near-field data in Figure 2, these measurements show that Ga^+-irradiated regions undergo a modified IMT: the transition is strongly suppressed (with higher doses effectively quenching it in the irradiated area), the metallic state becomes more resistive, and the insulating state becomes more conductive. When the lightly irradiated 0.2 pC μm^{-2} device is heated, the whole film easily changes phase. For higher dose irradiation (10 and 50 pC μm^{-2}) heating does not seem to switch the phase of the irradiated regions, suggesting potential defect-induced amorphization, which can suppress the phase transition and lower the phase transition temperature [14]. We also note that the near-field amplitude ratio is small in Figure 3b (maximum ≈0.3) when the device is switched using voltage compared to Figure 2d where a heater was used (maximum ≈0.8). This suggests that because s-SNOM is sensitive to surface conductivity changes, the onset of current in the voltage-exposed case corresponds to the device becoming conductive/metallic at the surface. In contrast, in the heated sample, the bulk of the film transitioned to a metallic phase, potentially leading to higher near-field amplitude contrast.

Terahertz nanoimaging enables diffraction-unrestricted probing of conductivity in correlated electron systems by providing high sensitivity to local variations in free carrier concentration associated with the IMT. We used broadband THz time-domain nanoimaging to investigate a 0.2 pC μm^{-2} Ga^+ ion-irradiated VO_2 thin film, revealing voltage-driven phase transitions and local conductivity changes at 0, 9, and 38 V, as shown in Figure 4a and Figure S9b. The near-field broadband THz amplitude images in panel 4(a) show voltage-dependent, reversible changes in conductivity. The spatial non-uniformity in the near-field signal at a fixed voltage is not evident in the line profiles in panel 4(b), which is attributed to both lack of resolution due to THz tips used as well as a uniform local THz scattering response of the film. Figure 4c shows normalized second harmonic amplitudes for a 0.2 pC μm^{-2} Ga^+-irradiated device, comparing signals from irradiated (blue)

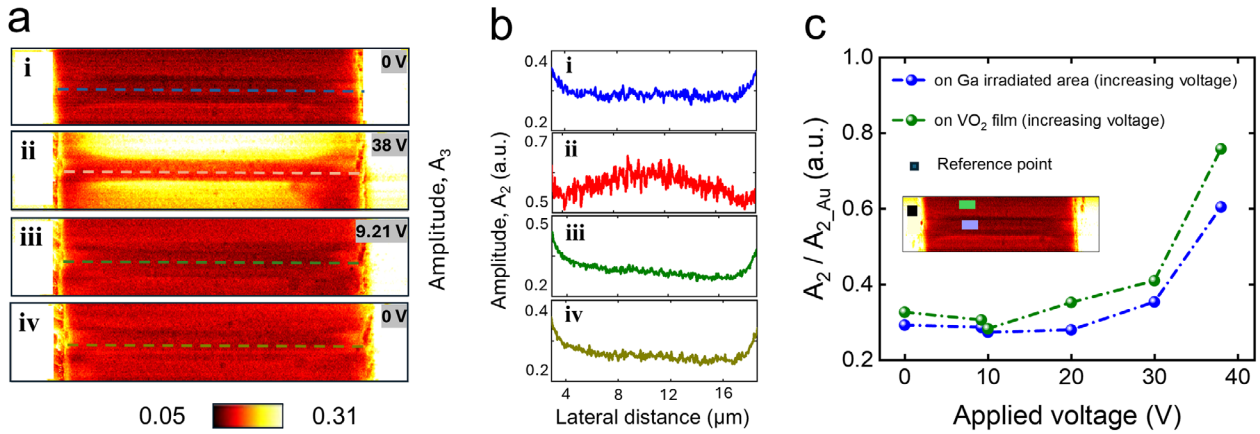

FIGURE 4 | Temperature-dependent THz nanoimaging of conductivity profiles in VO_2 thin films irradiated with a 0.2 pC μm^{-2} Ga^+ ion dose. (a) Broadband THz near-field amplitude images taken at (i) 0 V, (ii) 38 V, (iii) 9.21 V, and (iv) 0 V. (b) Line profiles extracted from the dashed lines in the amplitude images shown in (a)(i–iv). (c) Normalized second harmonic amplitude signal as a function of voltage, measured in the Ga^+-irradiated region (blue) and the pristine region (green). Scale bars represent 4 μm in (a).

and non-irradiated (green) regions during both increasing and decreasing voltages. The normalized amplitude in both the Ga^+-irradiated and pristine regions gradually increases, though the transition is slightly suppressed for the irradiated region. The THz mapping captures the device's hysteretic behavior as the voltage is decreased (Figure S10). The normalized amplitude values for the pristine VO_2 film area are greater than that of the irradiated area for both increasing and decreasing voltages, similar to results observed in the IR in Figure 3. Another important distinction between THz and IR responses lies in the slower rise of the normalized near-field amplitude signal at THz frequencies. At THz frequencies, the metallic state and the insulating state contrast increases gradually to ≈1.3, whereas in the IR it changes abruptly, exceeding a ratio of 3. This slower rise at THz implies stronger scattering even from low concentrations of free carriers. The underlying mechanism is linked to the behavior of the plasma frequency (see Figure S11), which shifts to higher energies for large carrier densities and to lower energies for smaller ones. As a result, the THz amplitude change remains gradual when transitioning from insulating to metallic regions, since low carrier density regions continue to scatter strongly [44]. This leads to a small and relatively constant contrast in THz between low- and high-carrier-density regions. In contrast, higher frequencies (IR and above) exhibit a large, abrupt amplitude difference between insulating and metallic regions—corresponding to small and large carrier concentrations, respectively—enabling clearer distinction between the two phases.

3 | Conclusion

We investigated how focused Ga^+ ion beam irradiation modulates the insulator–metal transition (IMT) and electronic properties of VO_2 thin films at the nanoscale, relevant for neuromorphic device architectures. Near-field nanoimaging reveals nanoscale, dose-dependent control of the IMT: irradiated filaments are more conductive than pristine VO_2 below the transition temperature but become more resistive at elevated temperatures. Consequently, irradiation suppresses thermal and electrical switching, yielding higher resistance than pristine VO_2 above the IMT. Our results further reveal a distinct contrast in behaviors in IR and THz responses due to their respective sensitivities to carrier density and scattering mechanisms. Together, these findings provide a better understanding of nanoscale phase engineering in defective correlated oxides and could be extended to other materials exhibiting nonvolatile resistive switching behavior at the IMT, thus offering a route toward reconfigurable, energy-efficient devices based on programmable quantum materials.

4 | Methods

4.1 | Nanoscale Imaging

For obtaining the nanoscale topography and near-field amplitude images of Ga irradiated VO_2 thin film devices, we utilized a s-SNOM configuration in which a platinum–iridium-coated atomic force microscope (AFM) tip oscillating at a resonance frequency of ≈280 KHz, was illuminated by a focused laser of wavelength, $\lambda = 10.5$ μm (E_{inc}) at 45° with respect to the sample. A parabolic mirror was used to focus the illumination laser to the tip-sample interface region, and the same mirror was used to collect the scattered light (E_{scat}) from that region. The excitation laser was polarized perpendicular to the plane of incidence (s-polarized), and the scattered signal was detected in the plane of incidence (p-polarized). The scattered signal from the tip-sample interface was demodulated at higher harmonics of the tip frequency to suppress background and detected via pseudo-heterodyne interferometry. By raster scanning the sample surface, concurrent topographical and near-field optical amplitude images were recorded.

4.2 | VO_2 Film Growth and Device Fabrication

VO_2 thin films, 40 nm in thickness, were grown on R-cut Al_2O_3 sapphire substrates by reactive radio frequency magnetron sputtering from a V_2O_3 target [14]. The deposition of VO_2 thin films was carried out in an atmosphere of 3.6 mTorr of Ar/O_2 (93/7%) at a substrate temperature of 470°C, employing reactive RF magnetron sputtering from a V_2O_3 target. After growth, the VO_2

samples were kept in the same atmosphere and cooled at a rate of 12°C min^{-1}. (100 nm Au)/(20 nm Ti) electrodes were fabricated in a two-terminal geometry using standard photolithography techniques. The 40 nm thickness was selected to preserve a pronounced and reproducible insulator to metal transition while providing substantial overlap between the VO_2 layer and the depth distribution produced by 30 keV Ga^+ irradiation. R-cut sapphire was selected as a stable, electrically insulating substrate that supports reproducible VO_2 growth and is compatible with the infrared and terahertz measurements used in this study.

4.3 | Focused Ion Beam Irradiation

Spatially selective irradiation was performed using a Ga^+ focused ion beam operated at an accelerating energy of 30 keV. The ion energy was held constant for all samples, and the areal dose was varied between 0.2, 10, and 50 pC μm^{-2}. Irradiated strips approximately 1 µm wide were patterned across the VO_2 channel. The 30 keV energy was selected because the calculated retained Ga^+ and primary displacement distributions overlap with a substantial fraction of the 40 nm VO_2 film. Other ion energies were not experimentally investigated. Ga^+ was selected because the available FIB platform provides mask-free, direct-write spatial modification and because the same ion species has previously been used to modify the VO_2 transition and localize resistive switching in VO_2 and V_2O_3 [14, 28, 30]. Also, Ga^+ irradiation was used just as a prototypical case and that similar effects have been observed in VO_2 irradiated with different ion beams (oxygen, helium, etc.) [39]. Thus, we believe that this effect does not Ga irradiation specific and is general irradiation by different ions.

Acknowledgements

This work was supported by the Gordon and Betty Moore Foundation, and the Air Force Office of Scientific Research (AFOSR) grant number FA9550-26-1B202.

Conflicts of Interest

The authors declare no conflicts of interest.

Data Availability Statement

The data that support the findings of this study are available from the corresponding author upon reasonable request.

References

1. H.-T. Zhang, T. J. Park, A. N. Islam, et al., "Reconfigurable Perovskite Nickelate Electronics for Artificial Intelligence," *Science* 375, no. 6580 (2022): 533–539, https://doi.org/10.1126/science.abj7943.

2. J. J. Yang, D. B. Strukov, and D. R. Stewart, "Memristive Devices for Computing," *Nature Nanotechnology* 8, no. 1 (2013): 13–24, https://doi.org/10.1038/nnano.2012.240.

3. J. Del Valle, J. G. Ramírez, M. J. Rozenberg, and I. K. Schuller, "Challenges in Materials and Devices for Resistive-Switching-Based Neuromorphic Computing," *Journal of Applied Physics* 124, no. 21 (2018): 211101, https://pubs.aip.org/aip/jap/article/124/21/211101/156058.

4. Y. Zhou and S. Ramanathan, "Mott Memory and Neuromorphic Devices," *Proceedings of the IEEE* 103, no. 8 (2015): 1289–1310, https://doi.org/10.1109/JPROC.2015.2431914.

5. E. Qiu, Y. H. Zhang, M. D. Ventra, and I. K. Schuller, "Reconfigurable Cascaded Thermal Neuristors for Neuromorphic Computing," *Advanced Materials* 36, no. 6 (2024): 2306818, https://doi.org/10.1002/adma.202306818.

6. E. Kisiel, P. Salev, I. Poudyal, et al., "High-Resolution Full-Field Structural Microscopy of the Voltage-Induced Filament Formation in VO_2-Based Neuromorphic Devices," *Acs Nano* 19, no. 16 (2024): 15385–15394, https://doi.org/10.1021/acsnano.4c14696.

7. A. Hoffmann, S. Ramanathan, J. Grollier, et al., "Quantum Materials for Energy-Efficient Neuromorphic Computing: Opportunities and Challenges," *APL Materials* 10, no. 7 (2022): 070904, https://pubs.aip.org/aip/apm/article/10/7/070904/2834975.

8. M. D. Pickett, G. Medeiros-Ribeiro, and R. S. Williams, "A Scalable Neuristor Built With Mott Memristors," *Nature Materials* 12, no. 2 (2013): 114–117, https://doi.org/10.1038/nmat3510.

9. A. Beck, J. Bednorz, C. Gerber, C. Rossel, and D. Widmer, "Reproducible Switching Effect in Thin Oxide Films for Memory Applications," *Applied Physics Letters* 77, no. 1 (2000): 139–141, https://doi.org/10.1063/1.126902.

10. S. Gamage, S. Manna, M. Zajac, et al., "Infrared Nanoimaging of Hydrogenated Perovskite Nickelate Memristive Devices," *ACS Nano* 18, no. 3 (2024): 2105–2116, https://doi.org/10.1021/acsnano.3c09281.

11. H. J. Conley, B. Wang, J. I. Ziegler, R. F. Haglund Jr, S. T. Pantelides, and K. I. Bolotin, "Bandgap Engineering of Strained Monolayer and Bilayer MoS_2," *Nano Letters* 13, no. 8 (2013): 3626–3630, https://doi.org/10.1021/nl4014748.

12. R. Wu, H. Zhang, H. Ma, et al., "Synthesis, Modulation, and Application of Two-Dimensional TMD Heterostructures," *Chemical Reviews* 124, no. 17 (2024): 10112–10191, https://doi.org/10.1021/acs.chemrev.4c00174.

13. M. Ghafariasl, T. Zhang, Z. D. Ward, et al., "Sulfur Vacancy Related Optical Transitions in Graded Alloys of $Mo_xW_{1-x}S_2$ Monolayers," *Advanced Optical Materials* 12, no. 11 (2024): 2302326, https://doi.org/10.1002/adom.202302326.

14. N. Ghazikhanian, J. del Valle, P. Salev, et al., "Resistive Switching Localization by Selective Focused Ion Beam Irradiation," *Applied Physics Letters* 123, no. 12 (2023): 123505, https://pubs.aip.org/aip/apl/article/123/12/123505/2911832.

15. D. N. Basov, R. D. Averitt, D. Van Der Marel, M. Dressel, and K. Haule, "Electrodynamics of Correlated Electron Materials," *Reviews of Modern Physics* 83, no. 2 (2011): 471–541, https://doi.org/10.1103/RevModPhys.83.471.

16. C. McGahan, S. Gamage, J. Liang, et al., "Geometric Constraints on Phase Coexistence in Vanadium Dioxide Single Crystals," *Nanotechnology* 28, no. 8 (2017): 085701, https://doi.org/10.1088/1361-6528/aa5652.

17. M. Imada, A. Fujimori, and Y. Tokura, "Metal-Insulator Transitions," *Reviews of Modern Physics* 70, no. 4 (1998): 1039–1263, https://doi.org/10.1103/RevModPhys.70.1039.

18. F. Morin, "Oxides Which Show a Metal-to-Insulator Transition at the Neel Temperature," *Physical Review Letters* 3, no. 1 (1959): 34–36, https://doi.org/10.1103/PhysRevLett.3.34.

19. J. Zhang, Z. Zhao, J. Li, et al., "Evolution of Structural and Electrical Properties of Oxygen-Deficient VO_2 Under Low Temperature Heating Process," *ACS Applied Materials & Interfaces* 9, no. 32 (2017): 27135–27141, https://doi.org/10.1021/acsami.7b05792.

20. S. M. Bohaichuk, M. Muñoz Rojo, G. Pitner, et al., "Localized Triggering of the Insulator-Metal Transition in VO_2 Using a Single Carbon Nanotube," *ACS Nano* 13, no. 10 (2019): 11070–11077, https://doi.org/10.1021/acsnano.9b03397.

21. B. Wang, R. Peng, X. Wang, et al., "Ultrafast, Kinetically Limited, Ambient Synthesis of Vanadium Dioxides Through Laser Direct Writing on Ultrathin Chalcogenide Matrix," *ACS Nano* 15, no. 6 (2021): 10502–10513, https://doi.org/10.1021/acsnano.1c03050.

22. B. R. Naik, D. Verma, and V. Balakrishnan, "Effect of Chemical Doping on Memristive Behavior of VO_2 Microcrystals," *Applied Physics Letters* 120, no. 6 (2022): 062101, https://pubs.aip.org/aip/apl/article/120/6/062101/2833065.

23. M. Belyaev, A. Velichko, V. Putrolaynen, and V. Perminov, "Electron Beam Modification of Vanadium Dioxide Oscillators," *Physica Status Solidi c* 14, no. 3-4 (2017): 1600236, https://doi.org/10.1002/pssc.201600236.

24. N. D'Anna, N. Ghazikhanian, E. S. Lamb, et al., "Self-Strain Suppression of the Metal-to-Insulator Transition in Phase-Change Oxide Devices," *Small* 22 (2025): 09287, https://onlinelibrary.wiley.com/doi/10.1002/smll.202509287.

25. W. Yi, K. K. Tsang, S. K. Lam, X. Bai, J. A. Crowell, and E. A. Flores, "Biological Plausibility and Stochasticity in Scalable VO_2 Active Memristor Neurons," *Nature Communications* 9, no. 1 (2018): 4661, https://doi.org/10.1038/s41467-018-07052-w.

26. Y.-H. Zhang, C. Sipling, E. Qiu, I. K. Schuller, and M. Di Ventra, "Collective Dynamics and Long-Range Order in Thermal Neuristor Networks," *Nature Communications* 15, no. 1 (2024): 6986, https://doi.org/10.1038/s41467-024-51254-4.

27. E. Qiu, P. Salev, F. Torres, H. Navarro, R. C. Dynes, and I. K. Schuller, "Stochastic Transition in Synchronized Spiking Nanooscillators," *Proceedings of the National Academy of Sciences* 120, no. 38 (2023): 2303765120, https://doi.org/10.1073/pnas.2303765120.

28. L. A. Giannuzzi, *Introduction to Focused Ion Beams: Instrumentation, Theory, Techniques and Practice* (Springer Science & Business Media, 2006), https://link.springer.com/book/10.1007/b101190.

29. K. Höflich, G. Hobler, F. I. Allen, et al., "Roadmap for Focused Ion Beam Technologies," *Applied Physics Reviews* 10, no. 4 (2023): 041311, https://pubs.aip.org/aip/apr/article/10/4/041311/2931107.

30. H. Mei, A. Koch, C. Wan, et al., "Tuning Carrier Density and Phase Transitions in Oxide Semiconductors Using Focused Ion Beams," *Nanophotonics* 11, no. 17 (2022): 3923–3932, https://doi.org/10.1515/nanoph-2022-0050.

31. Y. Kalcheim, A. Camjayi, J. Del Valle, P. Salev, M. Rozenberg, and I. K. Schuller, "Non-Thermal Resistive Switching in Mott Insulator Nanowires," *Nature Communications* 11, no. 1 (2020): 2985, https://doi.org/10.1038/s41467-020-16752-1.

32. H. Hofsäss, P. Ehrhardt, H.-G. Gehrke, et al., "Tuning the Conductivity of Vanadium Dioxide Films on Silicon by Swift Heavy Ion Irradiation," *AIP Advances* 1, no. 3 (2011): 032168, https://pubs.aip.org/aip/adv/article/1/3/032168/19813.

33. J. Rensberg, S. Zhang, Y. Zhou, et al., "Active Optical Metasurfaces Based on Defect-Engineered Phase-Transition Materials," *Nano Letters* 16, no. 2 (2016): 1050–1055, https://doi.org/10.1021/acs.nanolett.5b04122.

34. R. Hillenbrand, Y. Abate, M. Liu, X. Chen, and D. Basov, "Visible-to-THz Near-Field Nanoscopy," *Nature Reviews Materials* 10, no. 4 (2025): 285–310, https://doi.org/10.1038/s41578-024-00761-3.

35. Y. Abate, D. Seidlitz, A. Fali, et al., "Nanoscopy of Phase Separation in $In_xGa_{1-x}N$ Alloys," *ACS Applied Materials & Interfaces* 8, no. 35 (2016): 23160–23166, https://doi.org/10.1021/acsami.6b06766.

36. J. F. Ziegler and J. P. Biersack, "The Stopping and Range of Ions in Matter," in Treatise on Heavy-ion: Volume *6*: Scienceastrophysics, Chemistry, and Condensed Matter (Springer, 1985), 93–129.

37. J. F. Ziegler, "SRIM-2003," *Nuclear Instruments and Methods in Physics Research Section B: Beam Interactions with Materials and Atoms* 219-220 (2004): 1027–1036, https://doi.org/10.1016/j.nimb.2004.01.208.

38. J. F. Ziegler, M. D. Ziegler, and J. P. Biersack, "SRIM–The Stopping and Range of Ions in Matter," *Nuclear Instruments and Methods in Physics Research Section B: Beam Interactions With Materials and Atoms* 268, no. 11-12 (2010): 1818–1823.

39. J. G. Ramirez, T. Saerbeck, S. Wang, et al., "Effect of Disorder on the Metal-Insulator Transition of Vanadium Oxides: Local versus Global Effects," *Physical Review B* 91, no. 20 (2015): 205123, https://doi.org/10.1103/PhysRevB.91.205123.

40. N. Ghazikhanian, D. J. Alspaugh, P. Salev, L. Fratino, M. Rozenberg, and I. K. Schuller, "Enhanced Stochasticity in Irradiated Vanadium Oxide Oscillators," *Advanced Functional Materials* (2026): e29777, https://advanced.onlinelibrary.wiley.com/doi/10.1002/adfm.202529777.

41. W. Lin, H. Zhang, Y. Kalcheim, et al., "Direct Visualization of Percolating Metal-Insulator Transition in V_2O_3 Using Scanning Microwave Impedance Microscopy," *Science China Physics, Mechanics & Astronomy* 65, no. 9 (2022): 297411, https://doi.org/10.1007/s11433-022-1932-9.

42. J. Del Valle, P. Salev, F. Tesler, et al., "Subthreshold Firing in Mott Nanodevices," *Nature* 569, no. 7756 (2019): 388–392, https://www.nature.com/articles/s41586-019-1159-6.

43. J. A. Hofer, A. C. Basaran, A. Pofelski, et al., "Ultrathin VO_2 Films on Functional Substrates," *ACS Applied Materials & Interfaces* 17, no. 15 (2025): 22992–23002, https://doi.org/10.1021/acsami.5c02682.

44. H. T. Stinson, A. Sternbach, O. Najera, et al., "Imaging the Nanoscale Phase Separation in Vanadium Dioxide Thin Films at Terahertz Frequencies," *Nature Communications* 9, no. 1 (2018): 3604, https://doi.org/10.1038/s41467-018-05998-5.

Supporting Information

Additional supporting information can be found online in the Supporting Information section.

Supporting File: adom71741-sup-0001-SuppMat.pdf.